



Effect of laser-wire interaction on bead characteristics at non-planar orientations during off-axis directed energy deposition

Sumitkumar Rathor¹ · Ekta Singla¹ · Ravi Kant¹

Received: 28 June 2024 / Accepted: 28 August 2024
© The Author(s), under exclusive licence to Springer Nature Switzerland AG 2024

Abstract

In the laser-wire directed energy deposition (LWDED) process, the laser-wire interaction (LWI) length directly influences wire melting and the deposition of a uniform layer. However, the effect of LWI length on bead morphology has not been studied due to the lack of a reliable method to calculate LWI length for off-axis wire feed systems. In this work, an analytical model is introduced to predict LWI length at non-planar orientations. The model development considers laser beam diameter, wire thickness, wire feed angles, and substrate tilt angles. It discusses the centre and trailing wire positions on the substrate. Single-bead-on-plate experiments were performed to present the effect of LWI length at non-planar orientations on bead geometry. The experimental findings reveal that the variations in substrate angles and wire feed angles influence bead width, height, and peak shift. The deposited bead geometry was investigated to demonstrate the effect of LWI and laser spot size. This work contributed to investigating the bead geometry at non-planar orientations for the off-axis wire-fed robotic LWDED process. At non-planar orientation, the predicted maximum LWI length was 1.07 mm at a 15° substrate angle and 10° wire feed angle. The melt pool depths were 336 μm, 261 μm, 290 μm, and 183 μm, respectively, with the corresponding laser energy densities of 29 J/mm³, 22 J/mm³, 25 J/mm³, and 16 J/mm³. These findings aid in deciding substrate positions and orientations in additive manufacturing (AM) of thin-walled overhang tubular parts and repair of conformal parts.

Keywords Laser-wire interaction · Non-planar orientation · Analytical model · Off-axis · Bead geometry · Additive manufacturing

List of symbols

α	Wire feed angle	ν	Laser scan speed
θ	Substrate tilt angle	S	Wire feed
ω	The angle between the laser head and the horizontal plane	r_0	Initial laser spot radius
ψ	The angle between laser head and the vertical plane	r	Laser spot radius at tilt position
β	Half divergence angle	q	Fixed angle between the wire nozzle and the laser head
P	Laser power	L_w	Laser-wire interaction length
f	Modulation frequency	D_{wire}	Wire diameter
d_0	Laser beam diameter	w	Bead width
D	Duty cycle	h	Bead height
		u	Bead peak shift

✉ Ravi Kant
ravi.kant@iitrpr.ac.in; only4ravikant@gmail.com

Sumitkumar Rathor
rathor.20mez0005@iitrpr.ac.in;
rathorsumitkumar@gmail.com

Ekta Singla
ekta@iitrpr.ac.in

¹ Department of Mechanical Engineering, Indian Institute of Technology Ropar, Rupnagar, Punjab 140001, India

1 Introduction

Additive manufacturing (AM) is recognized for producing complex parts for critical industry applications. It used 3D computer-aided design (CAD) models to produce parts rapidly [1]. AM process takes longer build time, support material, and dynamic adhesion strength between layers and substrate. These unique advantages and challenges affect

tensile strength, surface finish, and tribological properties [2–4]. Metal AM process categories include directed energy deposition (DED), powder bed fusion (PBF), and solid state (cold spray, friction stir deposition, ultrasonic AM) [5–7]. The DED process uses wire and powder as a feed material for planar and non-planar depositions. This technology can employ different polymer, ceramic, and metal alloys [8–10].

Laser-wire directed energy deposition (LWDED) is an advanced joining, surface modification, and AM process [11, 12]. The process deposits material when the substrate is horizontal (planar) or non-planar and the laser head is orthogonal or at an angle. Advances in this process introduced robotic assistance to control positions at non-planar orientations and to introduce new deposition strategies for building intricate geometries [13–15].

The feed materials in wire and powder form are supplied through a coaxial or off-axial nozzle to form a metallurgical bond with the surface [16, 17]. Off-axial wire feed LWDED is used for applications in aerospace, biomedical, and automobile industries due to its advantages, such as a small heat-affected zone (HAZ), high bonding strength, and low dilution rate [18, 19]. The mechanical properties and structure of the bead are not uniform over the entire length. The layer formation is influenced by different process parameters such as laser power, material feed rate, material feed angle, scan speed, and laser head tilt angle. These parameters are also important in achieving the desired geometrical surface finish for single-layer and multi-layer thin-walled parts. The position of the bead peak is influenced by gravity at non-planar orientations, affecting the surface finish of the deposited layer.

Laser-wire interaction is important as it is related to deposition quality. The deposition quality depends on the length of the LWI, which results in full, partial, or no melting [20, 21]. As the length of the material interacting with the laser increases, it absorbs more energy, increasing melting [22]. The distance the wire travels primarily influences the laser spot diameter and profile. Using different scanning strategies, LWDED can be used as laser cladding, thin-walled parts, and bulk multi-layer deposition.

The relationship between the bead geometry and process parameters investigated a single and multi-layer deposition in LWDED [23]. A local closed-loop architecture can also control bead geometry [24]. Roch et al. [25] investigated the influence of process parameters on bead geometry during single-layer deposition by changing the laser head orientation. Asymmetric beads form as the laser head is tilted at an angle. A machine learning-based numerical model was proposed to predict layer geometry via real-time molten pool data [26, 27]. However, only powder-based DED processes were studied analytically to establish and predict the relationship of bead geometry with a tilted nozzle head while keeping the substrate horizontal and tilted [28–32].

The wire-based DED process has not yet been investigated to find a relationship with wire feed angle, laser beam spot diameter, and bead width at non-planar orientations [33, 34]. The study of beads morphology on inclined substrates is not as well understood as on horizontal substrates. The wire feed angle and substrate tilt angle are significant variables in the off-axial method. LWI is directly responsible for forming beads after solidifying the melt pool on the substrate. An inclined substrate position can profoundly affect the bead morphology. It is imperative to consider LWI length when predicting the change in the bead morphology to achieve reliable and precise results [22]. The LWI directly influences the melting of the deposited material; hence, it must be predicted.

This work novelty establishes and discusses the relationship between LWI length, laser beam spot diameter, and bead width when depositing a single layer at non-planar orientations. A new analytical model for non-planar depositions is presented to predict the laser-wire interaction length in off-axial laser-based DED. This work is required to predict the next layer bead characteristics for the supportless thin-walled deposition at the non-planar configurations. Also, this work can be helpful in deciding the favourable build angles and their effect on repairing randomly broken parts like gear teeth, impeller blades, and supportless additive manufacturing of conformal geometry parts.

The remainder of the paper is structured as follows: Sect. 2 presents the experimental setup of the LWDED system and characterization methodology. Section 3 introduces the analytical description for the LWI length at the centre and trailing wire position. Section 4 discusses the experimental results and demonstrates the LWI prediction and complexity of non-planar orientations for bead geometry in the LEDED process. Section 5 analyses the reason for the LWI model at the trailing position. Section 6 provides conclusions and highlights the research contribution and future scope.

2 Experimental procedures

An in-house robotic laser-wire DED experimental setup was developed and used to conduct all the experiments, as shown in Fig. 1. The setup consists of an off-axial nozzle that feeds metal wire through a self-developed wire feeder. KUKA 6-DOF robot controls the motion with a fixed platform. The experimental setup uses a fibre laser with a wavelength of 1080 nm and a maximum power output of 1 kW.

The stainless steel 316L wire with a diameter of 0.8 mm was deposited on a mild steel substrate of 100 mm × 100 mm × 6 mm. The chemical compositions of the wire and substrate material were provided by the manufacturer and are listed in Table 1. The oxide layer on the substrate

Fig. 1 Laser-wire DED experimental setup developed for this study using a 6-DOF robotic system. The inset figure shows the single-layer deposition at substrate angle θ

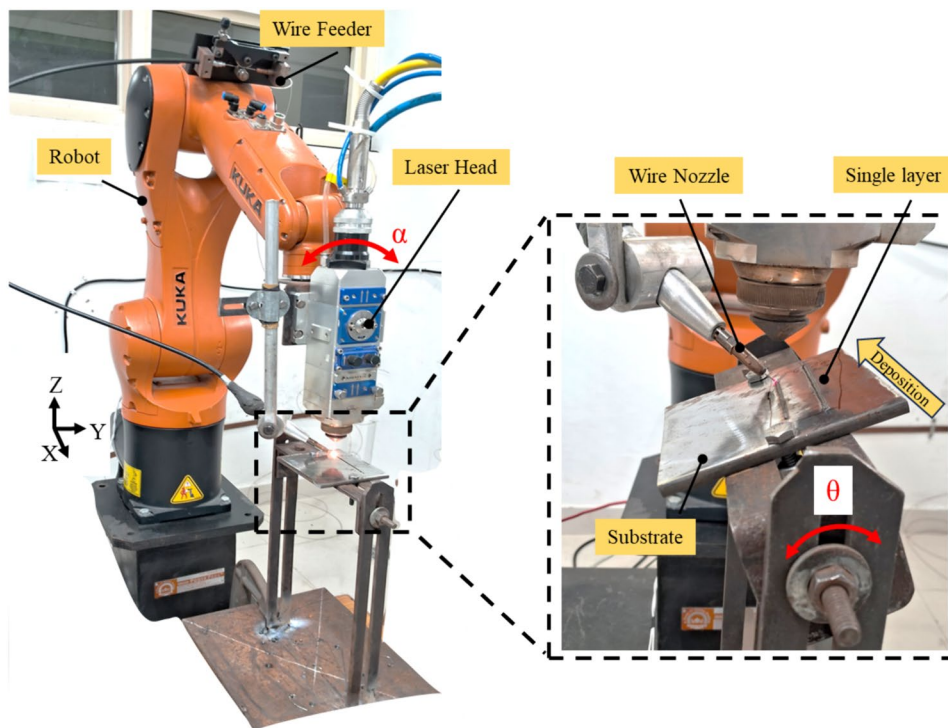


Table 1 Chemical composition of the wire and substrate used for this study

	Elements	Cr	Ni	Mo	Mn	Si	C	S	P	Fe
SS 316L	Wt.%	18.62	12.44	2.36	1.85	0.44	0.025	0.008	0.01	Bal
Mild steel	Wt.%	–	–	–	0.7	0.4	0.16	0.04	0.04	Bal

surface was removed and cleaned with ethanol before the single-layer experiment. This work investigates the non-planar orientations with the substrate angle (θ) and wire feed angle (α), as shown in Fig. 2 (a-d).

Primary geometric parameters used to characterize the bead morphology are width (w), height (h), and peak shift (u), as shown in Fig. 2 (e). The figure presents the cross section of a single layer when both the substrate and the laser head are tilted.

This work investigates the correlation between LWI length, laser spot profile, and bead width when depositing a single layer at non-planar orientations. So, it was not necessary to consider all parameters of the laser-wire DED process.

Table 2 presents the experiment design of the four-level substrate and wire feed angles while keeping the deposition parameters constant. The pulsed laser power (P) was 600 W, the laser beam diameter (d_0) was 1.8 mm, the modulation frequency (f) was 80 Hz, the duty cycle (D) was 50%, the laser scan speed (v) was 4 mm/s, and the wire feed (S) was 13 mm/s. The unidirectional deposition strategy was used to deposit the layers adjacently with

approximately 15 mm hatch spacing. Three sets of samples were prepared from each experiment.

The energy density for a pulsed laser can be given as [35]

$$\text{Laser energy density} = \frac{P_{\text{Peak}}}{A \times v} \frac{\text{J}}{\text{mm}^3} \tag{1}$$

Here, P_{Peak} is the peak laser pulse power (W), v is the deposition speed (mm/s), and A is the laser spot area. To calculate the laser spot area, laser spot diameter d can be expressed as follows:

$$d = d_0 \times \frac{\cos(\theta)}{\cos(\theta + \beta + (30 - \alpha))} \text{mm} \tag{2}$$

where d_0 is the initial laser bead diameter, θ is the substrate angle, α is the wire feed angle, and β is the half divergence angle. Optical images of the bead cross section were obtained by cutting, mounting, and polishing. The samples were chemically etched using a highly aggressive etchant aqua regia that can be used to reveal the grain structure of steel. It is a mixture of nitric acid and hydrochloric acid at a 1:3 ratio exposed for approximately 15 s. Microhardness

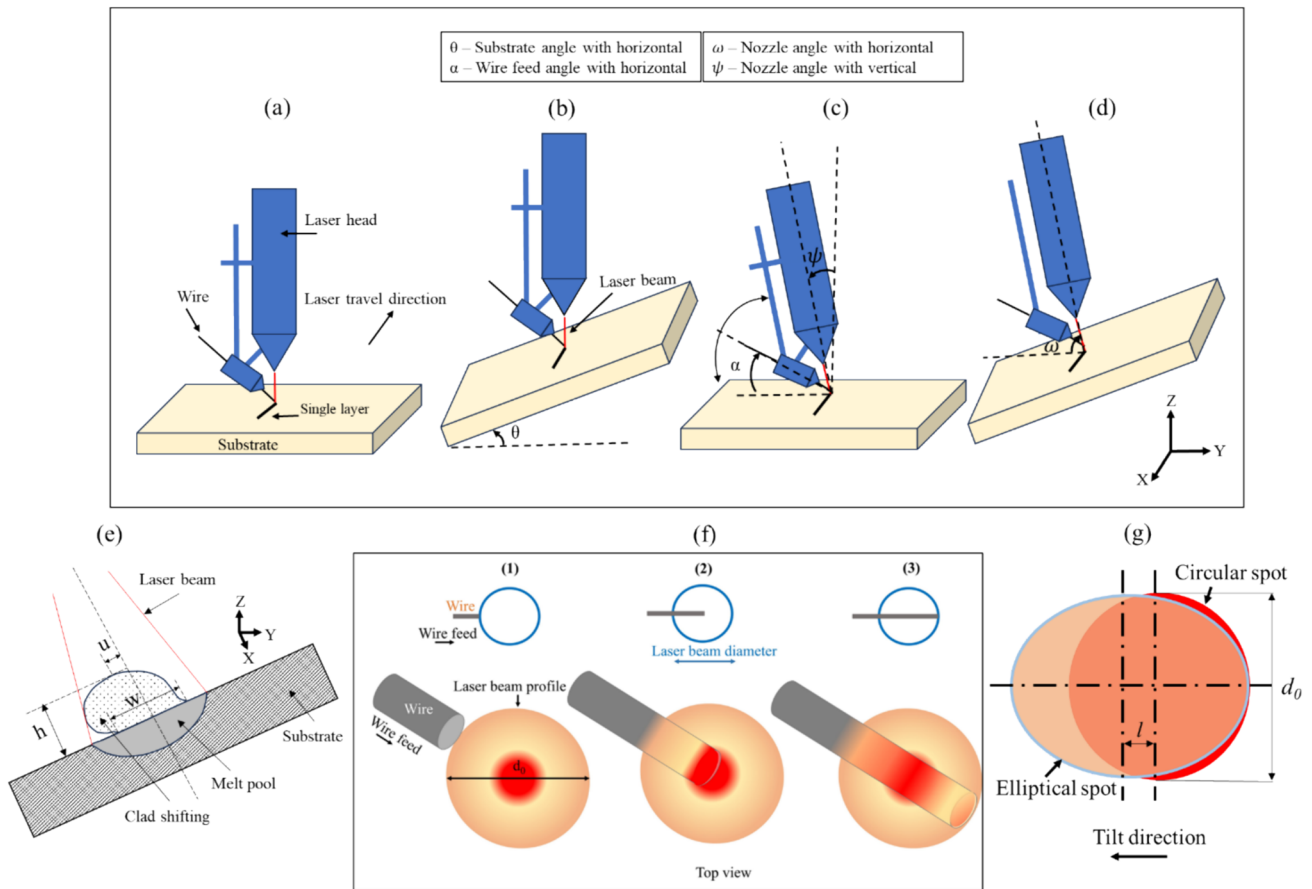


Fig. 2 Schematic showing different orientation configurations **a** substrate, nozzle, and wire at reference position **b** substrate at an angle **c** inclined wire feed nozzle **d** both substrate and wire feed nozzle inclined **e** Geometric parameters to characterize the bead morphol-

ogy on the inclined substrate **f** Different wire positions for interaction with the laser beam: (1) lead (2) centre, (3) trailing position **g** Laser spot shape change to elliptical shape at non-planar orientations

Table 2 Design of experiment

Experiment No	Substrate angle (θ°)	Wire feed angle (α°)
E1	0	10
E2	0	20
E3	0	30
E4	0	40
E5	15	10
E6	15	20
E7	15	30
E8	15	40
E9	30	10
E10	30	20
E11	30	30
E12	30	40
E13	45	10
E14	45	20
E15	45	30
E16	45	40

test was performed using Vickers hardness tester (WILSON 402MVD) with 100g load, 10 s dwell time, and 400 μm for each indent. The indentations were tested and reported in three sample sets, with a total of 30 indentations. Optical images were imported into open-source image processing software to measure the bead parameters.

3 Analytical model for laser-wire interaction length

3.1 Model description

The wire was fed off-axially to the substrate for laser-wire interaction through a nozzle. There are three different positions (i.e. lead, centre, and trailing) to have a wire interaction with the laser beam spot diameter d_0 , as shown in Fig. 2 (f). Besides, the horizontal substrate was tilted at an angle θ , and the diameter of the laser spot on the substrate increased [31]. Establishing the LWI model aids in finding such correlations

between LWI length, laser spot profile, and bead width of single-layer deposition of the non-planar LWDED process.

The laser spot profile changes when it is not perpendicular to the substrate, and the relationship can be discussed based on the sine theorem. The assumptions for representing the complete model during the interaction between the laser beam and the wire are as follows:

1. The laser beam appearance was conical.
2. The wire has a uniform size, and it was fed at a constant rate.
3. The wire feed nozzle was fixed to the laser head at a 60° angle.
4. The wire was fed up to the centre axis of the laser beam in Case 1, and the wire fed up to the trailing position of the laser beam diameter in Case 2 for the laser-wire interaction, as shown in Fig. 3 (a) and (b), respectively.

The relation of all the angles was established with α and θ from Fig. 3 (b). Using triangle BAC, the fixed angle between the wire and the laser head q was calculated as

$$\alpha + \theta + 180 - (\omega + \theta) = 180 + q,$$

$q = \alpha - \omega = -60$, minus sign indicates the angle direction and ω was the angle between the laser head and the horizontal plane.

In this study, the value of q was constant, and the relation of angles with α and θ was as follows:

$$\omega = 60 + \alpha, \tag{3}$$

$$\psi = 90 - \omega, \tag{4}$$

$$\psi + \alpha + 60 = 90, \tag{5}$$

$$\psi = 30 - \alpha, \tag{6}$$

where ψ was the angle between the laser head and the vertical plane as shown in Fig. 2 (c).

3.2 Laser-wire interaction length for Case 1: centre wire position

The wire fed to the substrate interacts with the laser to get melted when the laser energy is absorbed, and the melt pool solidifies on the substrate to form a layer. Figure 3 (a) shows the schematic of the wire positioned at the centre of the laser beam diameter.

In triangle OCD, angle D (θ_D) was calculated as

$$\beta + (\omega + \theta) + \theta_D = 180,$$

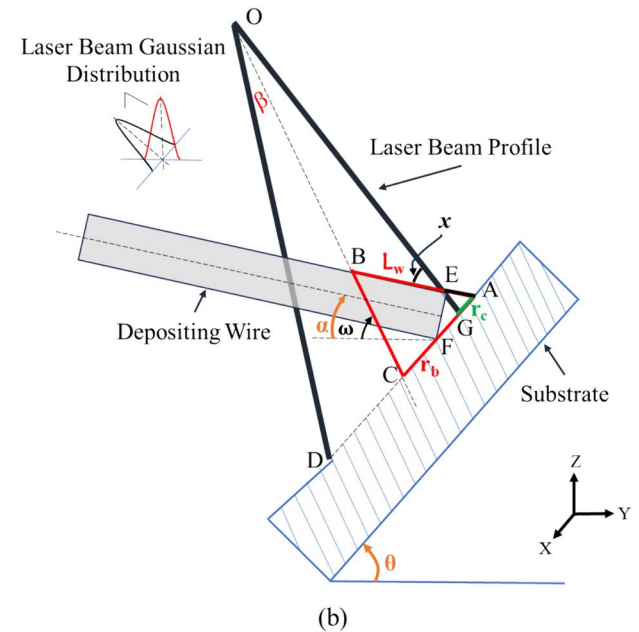
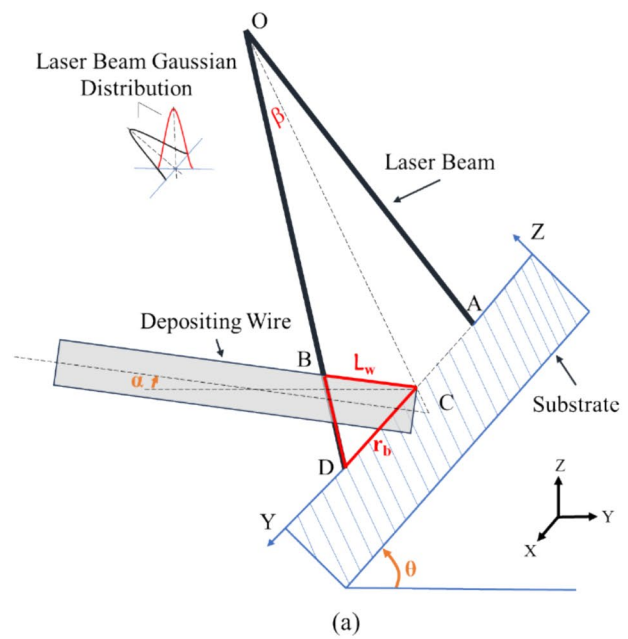


Fig. 3 Schematic showing the wire length in contact with the laser on the inclined substrate for a Case 1 and b Case 2

$$\theta_D = 180 - (\beta + \omega + \theta).$$

Using the sine theorem and Eqs. (3), (4), (5), and (6), the LWI length L_w was expressed as follows:

$$\frac{L_w}{\sin(\theta_D)} = \frac{CD}{\sin(180 - (\theta_D + \theta + \alpha))}$$

$$\frac{L_w}{\sin(180 - (\beta + \omega + \theta))} = \frac{CD}{\sin(\beta + \omega - \alpha)}$$

$$L_w = r_b \times \frac{\sin(60 + \alpha + \beta + \theta)}{\sin(60 + \beta)} \quad (7)$$

3.3 Laser-wire interaction length for Case 2: trailing wire position

In this case, the position of the wire was touching the substrate at the trailing position shown in Fig. 3 (b). The length of the CD was neglected due to the large vertical distance between the substrate and the wire. So, it was assumed that there was no deposition at CD. Now, the LWI length was equal to the length BE,

$$L_w = BE, \\ BE = BA - EA.$$

Now, in triangle OEB, to find angle x was,

$$\alpha + 180 - (\alpha + 60 + \beta) + x = 180 \\ x = 60 + \beta \quad (8)$$

Using the sine theorem and Eq. (8), length EG was expressed in the triangle EGF as

$$EG = D_{\text{wire}} \times \frac{\cos(\alpha + \theta)}{\sin(60 + \alpha + \theta + \beta)} \quad (9)$$

This model considers the wire diameter D_{wire} fed to the substrate. Now the length $AG = r_c$ was expressed from triangle EAG as

$$r_c = EG \times \frac{\sin(60 + \beta)}{\sin(\alpha + \theta)} \quad (10)$$

$$r_b = r_0 \times \cos(30 - (\alpha + \theta)) \quad (11)$$

where the length $r_1 = r_c + r_b$. The triangle BAC and EAG express length BA and EA , respectively.

$$BA = \frac{2}{\sqrt{3}} \times r_1 \times \sin(120 - (\alpha + \theta)), \quad (12)$$

$$EA = r_c \times \frac{\sin(120 - (\alpha + \theta + \beta))}{\sin(60 + \beta)}. \quad (13)$$

The LWI length was expressed by subtracting Eqs. (12) and (13) as

$$L_w = \frac{2}{\sqrt{3}} \times r_1 \times \sin(120 - (\alpha + \theta)) - r_c \times \frac{\sin(120 - (\alpha + \theta + \beta))}{\sin(60 + \beta)}. \quad (14)$$

Further, the LWI length model expressed in Case 2 was considered for experiments investigating the relationship between laser beam spot shape and bead width.

4 Results

4.1 LWI length prediction

The LWI length was calculated through Eqs. (8–14) to find a relationship using the proposed analytical description. According to Eq. (14), in the LWI length prediction model and selected process parameters, Fig. 4 illustrates the predicted LWI length and experimentally measured width values. It can be seen from the figures that the predicted LWI length of a single layer was close to the measured width values. It demonstrates the effect of the LWI length on the bead width.

The increase in substrate angle resulted in a decrease in bead width. The LWI length prediction was more consistent with the measured bead width when the wire feed angle was 30° . The width initially increased at a substrate angle of 15° , followed by a decrease, except for the wire feed angle at 30° . The maximum predicted LWI length was observed for the 15° substrate angle and the minimum for the 45° substrate angle. The predicted LWI length, bead width, and laser spot profile were consistent with the substrate angle.

The longer LWI length results in a broader bead and reduced penetration depth. Figure 5 presents the bead cross section at which geometry is acceptable. The penetration depends on the laser energy density available during the experimental conditions. The change in LWI time and laser energy density affected the melt pool depth. The melt pool depth for experiments E8, E10, E11, and E14 was $336 \mu\text{m}$, $261 \mu\text{m}$, $290 \mu\text{m}$, and $183 \mu\text{m}$, respectively, with the corresponding laser energy density of 29 J/mm^3 , 22 J/mm^3 , 25 J/mm^3 , and 16 J/mm^3 . In experiment E11, where the wire feed angle equalled the substrate angle, and the wire was fed perpendicular to the substrate, cracks appeared at the bead–substrate interface. The fast-cooling rates using a pulsed laser led to the formation of brittle microstructures that promote cracking. The inset in Fig. 5 illustrates the martensite formation at the interface. The microhardness results shown in Fig. 6 reveal a uniform distribution along the bead area and the variation from interface to HAZ. The E14 experiment results in a minimum HAZ depth as less heat is transferred to the surrounding area due to lower laser energy density. Fine grain formation at higher laser energy density increases the microhardness near the interface area. The maximum microhardness was observed for the E8 experiment. In contrast, the minimum was observed for the E11 experiment, demonstrating the effect of laser energy density on microstructure formation. The shape of the melt pool area

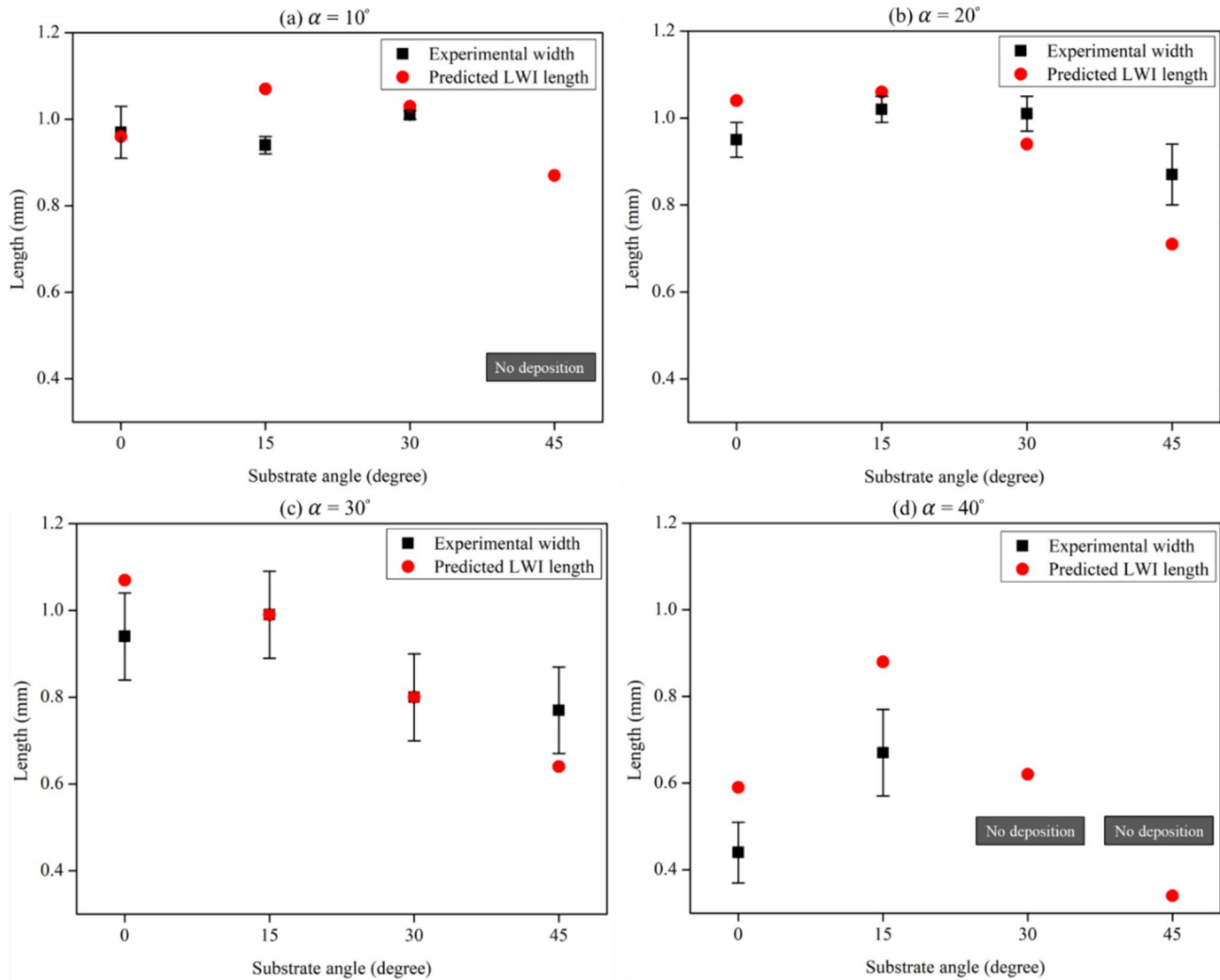


Fig. 4 Predicted values of LWI length compared with the experimentally measured width (w) at four wire feed angles (α), **a** 10° **b** 20° **c** 30° **d** 40°

changes with different laser spot shapes. The information on melt pool direction is helpful in selecting the layer height in multi-layer deposition.

4.2 Complexity of non-planar orientations

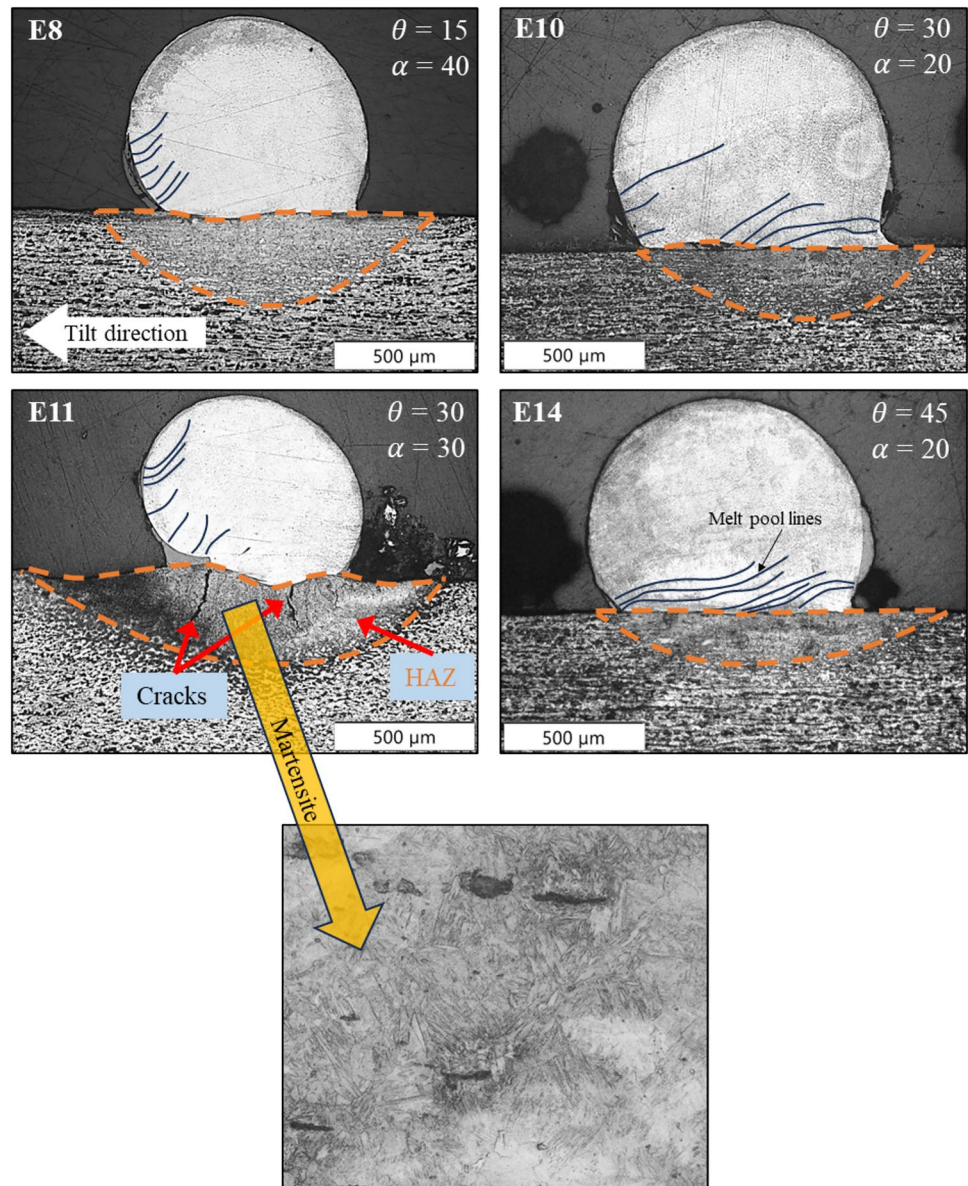
All the experiments were carried out at a single process parameter by changing the substrate angles to 0° , 15° , 30° , and 45° and the wire feed angles to 10° , 20° , 30° , and 40° . Melt pool geometry characteristics are not conspicuous when α and θ change with the horizontal plane. When the substrate was at 0° and the wire feed angle was at 10° , the bead height shifted in the direction of gravity, i.e. negative y , as shown in Fig. 2 (e). When the wire feed angle was increased, the peak shift was reduced at the same substrate angle. It was due to the increased solidification rate of using a pulsed laser at a lower frequency. Figure 2 (g) shows the

change in the laser spot profile on a tilted substrate. The laser spot position shifts by a distance of l , depending on the wire feed and substrate angles.

The melt pool solidification on an inclined surface with a non-orthogonal laser position helps us understand layer deposition. When the substrate angle is increased, the centre of laser energy density shifts towards the tilt direction by distance l . So, the solidification rate of the material at the shifted centre of the laser spot is lower in the tilt direction, which causes the material to fall towards the tilt direction before solidification. The laser spot profile at 30° substrate and wire feed angles gave the symmetrical bead profile. At this position, the laser spot profile was circular, resulting in minimal effect of gravity.

The bead profile exhibits significant sag when the laser spot centre is shifted with higher substrate angles. It is due to the concentration of the wire melt pool shifting towards

Fig. 5 The cross-sectional view of the bead showing changes in bead geometry at different non-planar orientations. The inset figure shows the martensite observed in HAZ and near the bead–substrate interface due to the high cooling rates of using a pulsed laser



the elevated side, gradually increasing the amount of molten material as the laser centre shifts at higher substrate angles.

A higher wire feed angle of 40° significantly affected the Bead width, as shown in Fig. 7 (a). It was due to the wire feeding from a higher angle, making less contact with the substrate and laser spot profile, which reduced the width length. The melted wire accumulates in a smaller area, reducing width and increasing height.

Discussing the significance of tilt angles in determining *bead height* is essential, as this aspect has yet to receive adequate attention. It was observed that the bead height decreases overall as the substrate angle increases as shown in Fig. 7 (b). The maximum height was observed for the E5 experiment condition, while the minimum was for E2. The maximum height was achieved when the substrate angle was

at 15° for both 10° and 20° wire angles. When the substrate angle was 30°, the height was similar for wire feed angles of 10°, 20°, and 30°. However, there was no deposition for the 40° wire feed angle when deposited at the 30° and 45° substrate angles.

The *peak shift* is related to the path planning of the multi-layer overhang part. When a new layer is added, it is built on top of the previous layer. Therefore, the bead shape or peak shift changes due to gravity in non-planar orientation. Figure 7 (c) shows the peak shift results for different wire feed angle and substrate angles. The peak shift for a 10° wire feed angle was almost the same due to reduced gravitational effects at the lower angle. As the substrate angle increases, the peak shift values gradually decrease. At a 30° substrate angle, the peak shift almost disappears. The minimum peak shift was

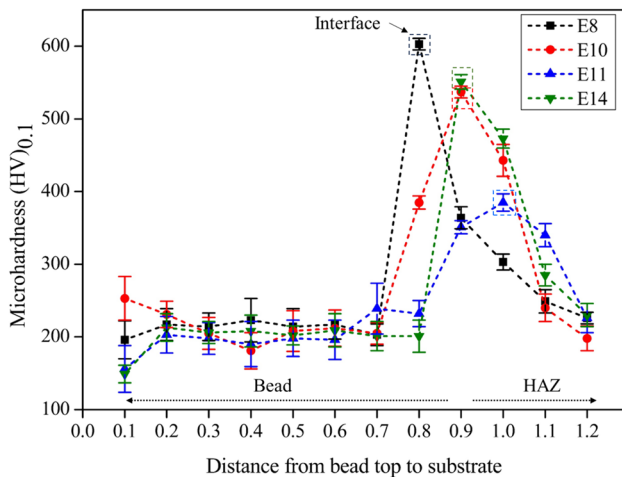


Fig. 6 Maximum microhardness at interface observed for E8 experiment demonstrating the effect of laser energy density on microstructure formation

observed in E11 when the laser beam was perpendicular to the substrate. Maximum peak shift was observed at a wire feed angle of 20° . However, at a substrate angle of 45° , the values are approximately similar because the effect of the wire feed angle on the bead parameter was minimal at this angle.

The *penetration depth* can vary based on the specific applications and materials used in LWDED. Earlier studies have shown that the penetration depth is over 0.2 mm with wire feed material and less than 0.02 mm with powder feed material at different orientations [32]. The beads with shallow penetration depths appeared at the extreme substrate and wire feed angles, as shown in Fig. 7 (d). A lower penetration depth at non-planar orientations can be due to laser irradiation into the substrate. The penetration depth is greater when the laser is orthogonal [36]. The higher difference between θ and α at non-planar configuration increases penetration depth. As previously discussed, the change in the laser spot profile reduces the laser trajectory, resulting in lower penetration depth. Using a pulsed laser leads to rapid cooling and solidification of the steel without deep heat penetration. The low penetration depth is beneficial as it reduces the remelting and recrystallization area in previously deposited layers.

The penetration depth and bead width decrease while the bead height increases with higher deposition angles. The dilution for all the processing conditions was calculated by considering the bead reinforcement and penetration areas [37]. A processing parameter condition that creates a deposit with a dilution $\leq 50\%$ was considered to produce thin-walled geometries. The dilution of single-layer track deposits in all the experiments was below 12%, as shown in Fig. 7 (e). Non-planar orientation does not affect dilution, while heat input and melting behaviour primarily drive the process.

5 Discussion

The change in substrate angle forms the elliptical laser spot size. The major length d of the ellipse was calculated using Eq. 2. The advantage of using wire is that there is no material flow distribution problem while depositing at non-planar orientations. The LWI length change and elliptical laser spot formation affected the bead morphology. The lower laser energy density was observed if the laser spot area increased. Similar results for microhardness in the HAZ region were observed for E10 and E14 experiments at a 20° wire feed angle.

It shows that the wire feed angle is significant to achieve repetitive results at different substrate angles. It is necessary to note that the laser energy density found no direct effect on bead morphology at non-planar orientations. It highlights the significance of the non-planar angles on bead geometry. The width, height, penetration depth, and peak shift were affected by changes in energy density as the substrate angle increased in the non-planar configuration. The diameter and shape of the laser spot affect the width of the bead. It was apparent that both angles could change the laser spot size. As the laser spot profile changes, the width of the melt pool also changes as it absorbs the laser power to form beads after solidification. One possible factor contributing to the bead width variation was the bead's shrinking due to surface tension effects. The laser beam interaction with the wire at increasing substrate angle introduced spattering, which causes deviations in the bead height. The shape of the melt pool can also get shifted because of the gravitational effect, which reduces bead height.

However, increasing the substrate angle reduces peak shift at a similar wire feed angle. The wire feed angle from the substrate surface increases at higher substrate angles. This means that the wire was being deposited from an angle closer to vertical. The effect of LWI length for predicting the bead morphology and toolpath planning was not considered in earlier studies [29, 38–40]. The results also demonstrate the significance of laser orientation for constructing thin-walled multi-layer overhang parts in industrial applications without requiring support structures.

6 Conclusion

This work established the relationship between LWI length, laser beam spot diameter, and bead width for the evolution of bead morphology at non-planar orientations during the robotic off-axial wire-fed LWDED process. An

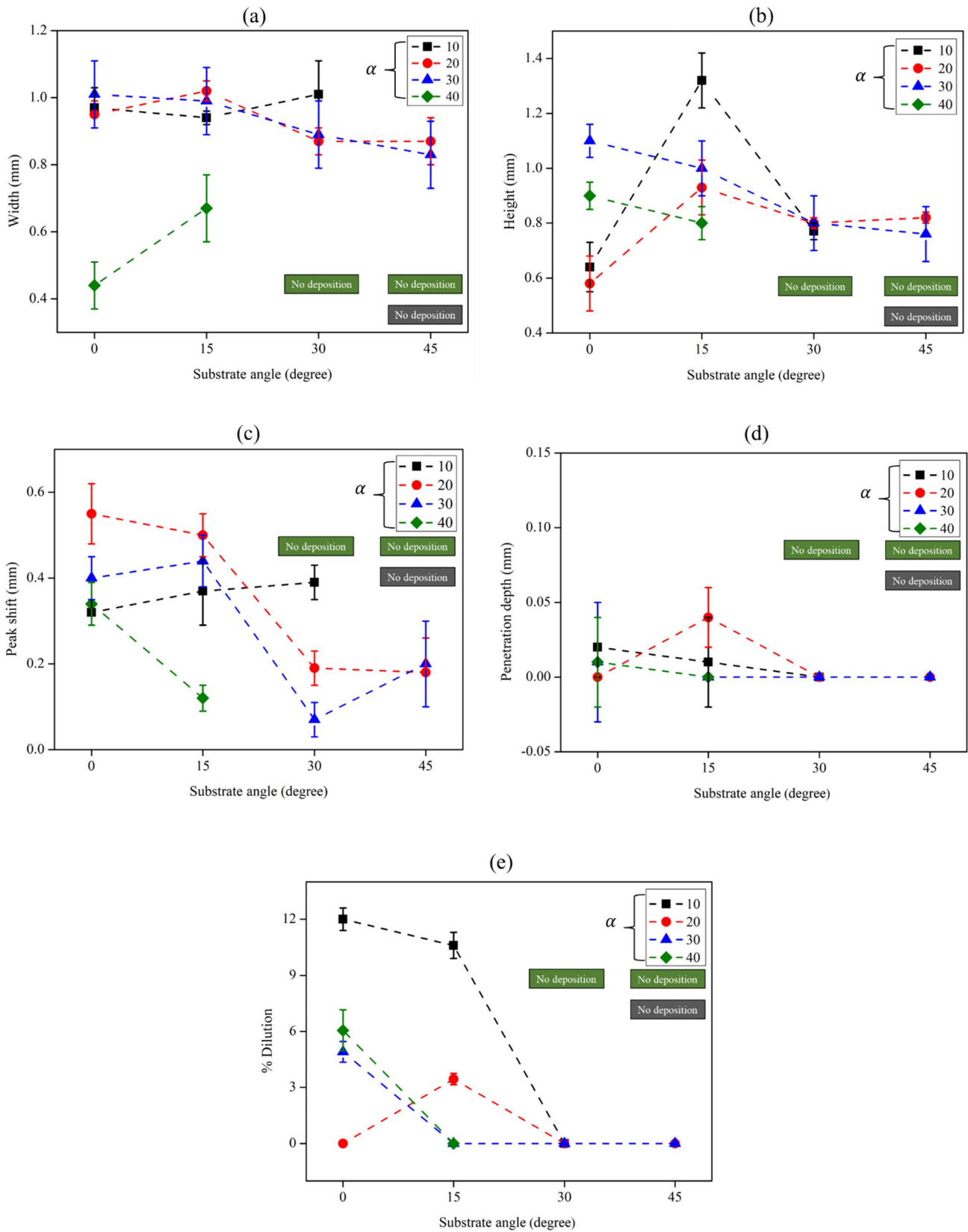


Fig. 7 The schematic showing the experimentally measured values of **a** width **b** height **c** peak shift **d** penetration depth **e** % dilution at respective substrate angle (θ) and wire feed angle (α)

analytical model was proposed to predict the LWI length at the off-axial nozzle position, considering laser beam diameter, wire thickness, wire feed angles, and substrate tilt angles. This model was discussed for the centre and trailing wire positions on the substrate. It investigated the effects of the wire feed angle α and the substrate angle θ on the width, height, and peak shift of the bead parameters. Experimental results present the relation between LWI length, laser beam diameter, and bead width. Higher wire feed angles tend to reduce bead width while increasing bead height due to reduced contact with the substrate.

The analytical model results revealed that the LWI prediction suits automatic toolpath planning in multi-axis LWDED. It is a new approach highlighting the significance of laser spot shape change with substrate angle and wire feed angle change to predict the changes in beads geometry at non-planar orientations. The minimum peak shift was observed for both θ and α at 30° , where the laser beam was perpendicular to the substrate, and the maximum peak shift was observed at a wire feed angle of 20° . The melt pool depths were $336\ \mu\text{m}$, $261\ \mu\text{m}$, $290\ \mu\text{m}$, and $183\ \mu\text{m}$, respectively, with the corresponding laser energy densities of $29\ \text{J}/\text{mm}^3$, $22\ \text{J}/\text{mm}^3$, $25\ \text{J}/\text{mm}^3$, and $16\ \text{J}/\text{mm}^3$. Single-layer deposition is influenced by heat input and melting behaviour at non-planar orientation on bead geometry and dilution. The fast-cooling rates using pulsed laser leads to the formation of brittle microstructure that promotes cracking.

The effect of LWI on multi-layer parts can be investigated further by varying the laser power, wire feed, and deposition speed. The morphological, mechanical, and thermal challenges in robotic LWDED can be addressed further to develop the path planning algorithm. Defining the angle limits suggested in this work results in collision avoidance to complete the deposition process. The substrate and wire feed angles can be further optimized to determine the orientation and position of the laser-wire interaction for interlayer adhesion. The procedure was proposed to calculate the LWI length, and discussion on the substrate and wire feed angle in this work can be used for path planning of repairing non-planar randomly broken parts like gear teeth, impeller blades, and supportless AM overhang geometry parts.

Acknowledgements This work was supported by the Department of Science and Technology (DST) through the project “Advanced Manufacturing Technology—Centre of Excellence (AMT-CoE) on Degradation Resistant Thermal Spray Coatings Engineered for Indigenous Industrial Applications (DST/TDT/AM/2022/143)” established at IIT Ropar.

Data availability All relevant data supporting the findings of this study are included within the manuscript.

Declarations

Conflict of interest The authors declare that there are no financial or non-financial interests.

References

- Rathor S, Kant R, Singla E (2023) Introduction to additive manufacturing. In: Kant R, Gurung H (eds) Industry 4.0. CRC Press, Boca Raton, pp 192–217
- De Oliveira D, Gomes MC, Dos Santos AG et al (2023) Abrasive and non-conventional post-processing techniques to improve surface finish of additively manufactured metals: a review. *Prog Addit Manuf* 8:223–240. <https://doi.org/10.1007/S40964-022-00325-3/METRICS>
- Ali HB, Ali HB, Shawish MH, Hasan SK (2023) Experimental investigation and statistical modelling for assessing the sliding wear of Futilized Filament Fabrication (FFF) fabricated parts. *Period Eng Nat Sci* 11(2):248–261
- Fadhil Abbas T, Basil Ali H, Kadhim Mansor K (2022) Influence of FDM process variables’ on tensile strength, weight, and actual printing time when using abs filament. *Int J Mod Manuf Technol* 14(1):7–13. <https://doi.org/10.54684/IJMMT.2022.14.1.7>
- Das A, Medhi T, Kapil S, Biswas P (2024) Multi-track multi-layer friction stir additive manufacturing of AA6061-T6 alloy. *Prog Addit Manuf* 9:835–855. <https://doi.org/10.1007/S40964-023-00485-W/METRICS>
- Kumar A, Rathor S, Vostrak M et al (2024) Exploring potential of cold spray technology for medical devices: Current and future scenario. *Mater Today Commun* 40:109534. <https://doi.org/10.1016/j.mtcomm.2024.109534>
- Zhang C, Yu H, Sun D, Liu W (2022) Ultrasonic additive manufacturing of metallic materials. *Met* 12(12):1912. <https://doi.org/10.3390/MET12111912>
- Ali HB, Oleiwi JK, Othman FM (2022) Compressive and tensile properties of ABS material as a function of 3D printing process parameters. *Rev des Compos des Mater Av* 32(3):117–123. <https://doi.org/10.18280/RCMA.320302>
- Li T, Tier L (2024) The influence of various factors on the 3D printing performance of cement-based materials was analyzed by geometric morphology. *Sadhana - Acad Proc Eng Sci* 49:1–9. <https://doi.org/10.1007/S12046-024-02443-W/FIGURES/9>
- Naik M, Thakur DG (2021) Experimental investigation of effect of printing parameters on impact strength of the bio-inspired 3D printed specimen. *Sadhana - Acad Proc Eng Sci* 46:1–9. <https://doi.org/10.1007/S12046-021-01671-8/FIGURES/13>
- Singh A, Kapil S, Das M (2020) A comprehensive review of the methods and mechanisms for powder feedstock handling in directed energy deposition. *Addit Manuf* 35:101388. <https://doi.org/10.1016/J.ADDMA.2020.101388>
- Li J, Zhou X, Brochu M et al (2024) Crystal introducing mechanism in laser wire directed energy deposition fabricated Ti6Al4V. *Prog Addit Manuf* 9:1–11. <https://doi.org/10.1007/s40964-024-00701-1>
- Kaji F, Jinoop AN, Zardoshtian A et al (2023) Robotic laser directed energy deposition-based additive manufacturing of tubular components with variable overhang angles: Adaptive trajectory planning and characterization. *Addit Manuf* 61:103366. <https://doi.org/10.1016/J.ADDMA.2022.103366>
- Rathor S, Kumar S, Singla E et al (2023) Robotic tool-path generation for complex and overhang-angled parts through offline programming. In: Singla E (ed) *Advances In Robotics - 6th International Conference of The Robotics Society*. ACM, New York, NY, USA, pp 1–5

15. Rathor S, Kumar A, Kant R, Singla E (2024) An overview of robot assisted additive manufacturing. In: Kant R (ed) *Modern Materials and Manufacturing Techniques*. CRC Press, Boca Raton, pp 154–179
16. Guner A, Bidare P, Jiménez A et al (2022) Nozzle designs in powder-based direct laser deposition: a review. *Int J Precis Eng Manuf* 23:1077–1094. <https://doi.org/10.1007/S12541-022-00688-1/FIGURES/19>
17. Herberger C, Heinrich L, LaNeave E et al (2024) Coaxial color channel focus evaluation to estimate standoff height in directed energy deposition additive manufacturing. *Prog Addit Manuf*. <https://doi.org/10.1007/S40964-024-00572-6/METRICS>
18. Saboori A, Aversa A, Marchese G et al (2019) Application of directed energy deposition-based additive manufacturing in repair. *Appl Sci* 9:3316. <https://doi.org/10.3390/APP9163316>
19. Oh WJ, Son Y, Do Sik S (2020) Effect of in-situ heat treatments on deposition characteristics and mechanical properties for repairs using laser melting deposition. *J Manuf Process* 58:1019–1033. <https://doi.org/10.1016/J.JMAPRO.2020.08.074>
20. Yu Y, Huang W, Wang G et al (2013) Investigation of melting dynamics of filler wire during wire feed laser welding. *J Mech Sci Technol* 27:1097–1108. <https://doi.org/10.1007/S12206-013-0218-4>
21. Ding D, Pan Z, Cuiuri D, Li H (2015) Wire-feed additive manufacturing of metal components: technologies, developments and future interests. *Int J Adv Manuf Technol* 81:465–481. <https://doi.org/10.1007/S00170-015-7077-3>
22. Noori Rahim Abadi SMA, Mi Y, Kisielewicz A et al (2023) Influence of laser-wire interaction on heat and metal transfer in directed energy deposition. *Int J Heat Mass Transf* 205:123894. <https://doi.org/10.1016/J.IJHEATMASSTRANSFER.2023.123894>
23. Gibson BT, Bandari YK, Richardson BS et al (2020) Melt pool size control through multiple closed-loop modalities in laser-wire directed energy deposition of Ti-6Al-4V. *Addit Manuf* 32:100993. <https://doi.org/10.1016/J.ADDMA.2019.100993>
24. Hu D, Kovacevic R (2003) Modelling and measuring the thermal behaviour of the molten pool in closed-loop controlled laser-based additive manufacturing. *Proc Inst Mech Eng Part B J Eng Manuf* 217:441–452. <https://doi.org/10.1243/095440503321628125>
25. Roch C, Tournier C, Lavernhe S (2023) Influence of process parameters and head orientation on bead geometry for coaxial wire laser additive manufacturing. *Mater Res Proc* 28:119–127. <https://doi.org/10.21741/9781644902479-14>
26. Jamnikar ND, Liu S, Brice C, Zhang X (2022) In-process comprehensive prediction of bead geometry for laser wire-feed DED system using molten pool sensing data and multi-modality CNN. *Int J Adv Manuf Technol* 121:903–917. <https://doi.org/10.1007/S00170-022-09248-3/FIGURES/9>
27. Schmid S, Krabusch J, Schromm T et al (2021) A new approach for automated measuring of the melt pool geometry in laser-powder bed fusion. *Prog Addit Manuf* 6:269–279. <https://doi.org/10.1007/s40964-021-00173-7>
28. Tan H, Fan W, Qian Y et al (2020) Influence of inclined substrate on process characteristics of directed energy deposition. *Opt Laser Technol* 129:106288. <https://doi.org/10.1016/J.OPTLASTEC.2020.106288>
29. Hao J, Meng Q, Li C et al (2019) Effects of tilt angle between laser nozzle and substrate on bead morphology in multi-axis laser cladding. *J Manuf Process* 43:311–322. <https://doi.org/10.1016/j.jmapro.2019.04.025>
30. Li X, Li T, Shi B et al (2020) The influence of substrate tilt angle on the morphology of laser cladding layer. *Surf Coatings Technol* 391:125706. <https://doi.org/10.1016/j.surfcoat.2020.125706>
31. Wang D, Li T, Shi B et al (2021) An analytical model of bead morphology on the inclined substrate in coaxial laser cladding. *Surf Coatings Technol* 410:126944. <https://doi.org/10.1016/j.surfcoat.2021.126944>
32. Elsayed O, Adapa VSK, Kersten S et al (2023) Effects of lead and lean in multi-axis directed energy deposition. *Int J Adv Manuf Technol* 125:5119–5134. <https://doi.org/10.1007/s00170-023-11085-x>
33. Li J, Li HN, Liao Z, Axinte D (2022) Overlapped wire-fed laser cladding on inclined surfaces: An analytical model considering gravity and a model application. *J Mater Process Technol* 304:117559. <https://doi.org/10.1016/J.JMATPROTEC.2022.117559>
34. Capello E, Colombo D, Previtali B (2005) Repairing of sintered tools using laser cladding by wire. *J Mater Process Technol* 164:990–1000. <https://doi.org/10.1016/j.jmatprotec.2005.02.075>
35. Rathor S, Kant R, Singla E (2024) Effect of laser energy density on bead characteristics in wire-DED. *Sādhanā* 49:104. <https://doi.org/10.1007/s12046-024-02472-5>
36. Yadav R, Goyal DK, Kant R (2023) How different coating conditions affect temperature and bend angle when laser bending mild steel sheet. *Lasers Eng* 55:103–115
37. Cai Y, Wang Y, Chen H, Xiong J (2024) Molten pool behaviors and forming characteristics in wire-laser directed energy deposition with beam oscillation. *J Mater Process Technol* 326:118326. <https://doi.org/10.1016/j.jmatprotec.2024.118326>
38. Chalvin M, Campocasso S, Hugel V, Baizeau T (2020) Layer-by-layer generation of optimized joint trajectory for multi-axis robotized additive manufacturing of parts of revolution. *Robot Comput Integr Manuf* 65:101960. <https://doi.org/10.1016/j.rcim.2020.101960>
39. Kaji F, Jinoop AN, Zimny M et al (2022) Process planning for additive manufacturing of geometries with variable overhang angles using a robotic laser directed energy deposition system. *Addit Manuf Lett* 2:100035. <https://doi.org/10.1016/j.addlet.2022.100035>
40. Mbodj NG, Abuabiah M, Plapper P et al (2021) Bead geometry prediction in laser-wire additive manufacturing process using machine learning: case of study. *Appl Sci* 11:11949. <https://doi.org/10.3390/app112411949>

Publisher's Note Springer Nature remains neutral with regard to jurisdictional claims in published maps and institutional affiliations.

Springer Nature or its licensor (e.g. a society or other partner) holds exclusive rights to this article under a publishing agreement with the author(s) or other rightsholder(s); author self-archiving of the accepted manuscript version of this article is solely governed by the terms of such publishing agreement and applicable law.